

Long-term and high frequency non-destructive monitoring of water stable isotope profiles in an evaporating soil column

Y. Rothfuss¹, S. Merz¹, J. Vanderborght¹, N. Hermes¹, A. Weuthen¹, A. Pohlmeier¹, H. Vereecken¹ and N. Brüggemann¹

[1]{Forschungszentrum Jülich GmbH, Institute of Bio- and Geosciences, Agrosphere Institute (IBG-3), Leo-Brandt-Straße, D-52425 Jülich, Germany}

Correspondence to: Y. Rothfuss (y.rothfuss@fz-juelich.de)

Abstract

The stable isotope compositions of soil water ($\delta^2\text{H}$ and $\delta^{18}\text{O}$) carry important information about the prevailing soil hydrological conditions and for constraining ecosystem water budgets. However, they are highly dynamic, especially during and after precipitation events. The classical method of determining soil water $\delta^2\text{H}$ and $\delta^{18}\text{O}$ at different depths, i.e., soil sampling and cryogenic extraction of the soil water, followed by isotope-ratio mass spectrometer analysis is destructive and laborious with limited temporal resolution. In this study, we present an application of method based on gas-permeable tubing and isotope-specific infrared laser absorption spectroscopy for *in situ* determination of $\delta^2\text{H}$ and $\delta^{18}\text{O}$. We conducted a laboratory experiment with an acrylic glass column filled with medium sand equipped with gas-permeable tubing at eight different soil depths. The soil column was initially saturated from the bottom, exposed to evaporation for a period of 290 days, and finally rewatered. Soil water vapor $\delta^2\text{H}$ and $\delta^{18}\text{O}$ were measured daily, sequentially for each depth. Soil liquid water $\delta^2\text{H}$ and $\delta^{18}\text{O}$ were inferred from the isotopic values of the vapor assuming thermodynamic equilibrium between liquid and vapor phases in the soil. The experimental setup allowed following the evolution of typical exponential-shaped soil water $\delta^2\text{H}$ and $\delta^{18}\text{O}$ profiles with unprecedentedly high temporal resolution. As the soil dried, we could also show for the first time the increasing influence of the isotopically depleted ambient water vapor on the isotopically enriched liquid water close to the soil surface (i.e.,

1 atmospheric invasion). Rewatering at the end of the experiment led to instantaneous resetting
2 of the stable isotope profiles, which could be closely followed with the new method.

3 From simple soil $\delta^2\text{H}$ and $\delta^{18}\text{O}$ gradients calculations, we showed that the gathered data
4 allowed to determinate the depth of the Evaporation Front (EF) and how it receded into the
5 soil overtime. It was inferred that after 290 days under the prevailing laboratory air
6 temperature, moisture, and aerodynamic conditions, and given the specific hydraulic
7 properties of the sand, the EF had moved down to an approximate depth of -0.06 m. Finally,
8 data was used to test the expression for the slope of evaporation lines proposed by Gat (1971)
9 and based on the model of Craig and Gordon (1965). A very good agreement was found
10 between measured and simulated values (Nash and Sutcliffe Efficiency - NSE = 0.92) during
11 the first half of the experiment, i.e., until the EF reached a depth of -0.04 m. From this point,
12 calculated kinetic effects associated with the transport of isotopologues in the soil surface air
13 layer above the EF provided slopes lower than observed. Finally, values of isotope kinetic
14 effects that provided the best model-to-data fit (NSE > 0.9) were obtained from inverse
15 modelling, highlighting uncertainties associated with the determinations of isotope kinetic
16 fractionation and soil relative humidity at the EF.

17

18 **1 Introduction**

19 Stable isotopologues of water, namely $^1\text{H}^2\text{H}^{16}\text{O}$ and $^1\text{H}_2^{18}\text{O}$ are powerful tools used in a wide
20 range of research disciplines at different and complementary temporal and spatial scales. They
21 provide ways of assessing the origin of water vapor (e.g., Craig, 1961; Liu et al., 2010),
22 solving water balances of lakes (Jasechko et al., 2013) and studying groundwater recharge
23 (Blasch and Bryson, 2007; Peng et al., 2014). Analysis of the isotope compositions ($\delta^2\text{H}$ and
24 $\delta^{18}\text{O}$) of soil surface and leaf waters allows for partitioning evapotranspiration into
25 evaporation and transpiration (e.g., Dubbert et al., 2013; Hu et al., 2014; Rothfuss et al., 2012;
26 Yopez et al., 2005).

27 Moreover, from soil water $\delta^2\text{H}$ and $\delta^{18}\text{O}$ profiles, it is also possible to derive quantitative
28 information, such as soil evaporation flux, locate evaporation fronts, and root water uptake
29 depths (Rothfuss et al., 2010; Wang et al., 2010). Zimmermann et al. (1967) and later Barnes
30 and Allison (1983, 1984) and Barnes and Walker (1989) first analytically described soil
31 $^1\text{H}^2\text{H}^{16}\text{O}$ and $^1\text{H}_2^{18}\text{O}$ movement at steady / non-steady state and in isothermal/ non-isothermal
32 soil profiles. Between precipitation events, the soil water $\delta^2\text{H}$ and $\delta^{18}\text{O}$ profiles depend on

1 flux boundary conditions, i.e., fractionating evaporation and non-fractionating capillary rise as
2 well as on soil properties (e.g., soil tortuosity). In a saturated soil, the isotope excess at the
3 surface due to evaporation diffuses back downwards, leading to typical and well documented
4 exponential-shaped $\delta^2\text{H}$ and $\delta^{18}\text{O}$ profiles. For an unsaturated soil, assuming in a first
5 approximation that isotope movement occurs in the vapor phase above the soil “evaporation
6 front” (EF) and strictly in the liquid phase below it, the maximal $\delta^2\text{H}$ and $\delta^{18}\text{O}$ values are no
7 longer observed at the surface but at the depth of EF. Above the EF, in the so-called “vapor
8 region”, according to Fick’s law, soil water $\delta^2\text{H}$ and $\delta^{18}\text{O}$ decrease towards the depleted
9 ambient atmosphere water vapor $\delta^2\text{H}$ and $\delta^{18}\text{O}$. Braud et al. (2005), Haverd and Cuntz (2010),
10 Rothfuss et al. (2012), Singleton et al. (2004), and Sutanto et al. (2012) implemented the
11 description of the transport of $^1\text{H}^2\text{H}^{16}\text{O}$ and $^1\text{H}_2^{18}\text{O}$ in physically based soil-vegetation-
12 atmosphere transfer (SVAT) models (HYDRUS 1D, SiSPAT-Isotope, Soil-Litter iso,
13 TOUGHREACT). In these models, movement of soil $^1\text{H}^2\text{H}^{16}\text{O}$ and $^1\text{H}_2^{18}\text{O}$ occur in both
14 phases below and above the EF, and heat and water transports are properly coupled.

15 However, these tools suffer from the comparison with other “traditional” methods developed
16 to observe and derive soil water state and transport. In contrast with soil water content and
17 tension measured by, e.g., time-domain reflectometry and tensiometry, isotope compositions
18 of soil water are determined either following destructive sampling or non-destructively but
19 with poor spatial and temporal resolution (i.e., with section cups in combination with
20 lysimeters for soil water tension higher than -600 hPa, e.g., Goldsmith et al., 2011, Litaor,
21 1988). This greatly limits their informative value. Only since recently, non-destructive
22 methodologies based on gas-permeable membrane and laser spectroscopy can be found in the
23 literature (Rothfuss et al., 2013; Herbstritt et al., 2012; Volkmann and Weiler, 2014, Gaj et
24 al., 2015).

25 The central objective of this study was to demonstrate that a direct application of the method
26 of Rothfuss et al. (2013) to a soil column would allow monitoring soil water $\delta^2\text{H}$ and $\delta^{18}\text{O}$
27 profiles in the laboratory with high temporal resolution and over a long time period. We will
28 demonstrate that the obtained isotope data can be used to locate the evaporation front as it
29 recedes into the soil during the experiment. Finally, data will be also used to test the
30 expression proposed by Gat (1971) and based on the Craig and Gordon (1965) of evaporation
31 lines’ slopes.

32

1 **2 Material and methods**

2 **2.1 Isotopic analyses**

3 Isotopic analysis of liquid water and water vapor was performed using a cavity ring-down
4 spectrometer (L1102-i, Picarro, Inc., Santa Clara, CA, USA), calibrated against the
5 international primary water isotope standards V-SMOW2, GISP, and SLAP by liquid water
6 injection into the vaporizer of the analyzer. Primary and working standards' isotope
7 compositions were measured at 17,000 ppmv water vapor mixing ratio (number of replicates
8 = 4, number of injections per replicate = 8). Mean values and standard deviations were
9 calculated omitting the first three values of the first replicate to account for a potential
10 memory effect of the laser spectrometer. The laser spectrometer's dependence on water vapor
11 mixing ratio was also investigated according to the method of Schmidt et al. (2010).
12 Hydrogen and oxygen isotope ratios of water are expressed in per mil (‰) on the
13 international "delta" scale as defined by Gonfiantini (1978) and referred to as $\delta^2\text{H}$ and $\delta^{18}\text{O}$,
14 respectively.

15 **2.2 Soil column and measurements**

16 The experiment was conducted in a 0.0057 m³ acrylic glass column (0.11 m i.d., 0.60 m
17 height, Fig. 1a). The bottom of the column consisted of a porous glass plate (10 μm < pore
18 size diameter < 16 μm (4th class), Robu® GmbH, Hattert, Germany) connected to a two-way
19 manual valve (VHK2-01S-06F, SMC Pneumatik GmbH, Germany).

20 Three ports were available at each of eight different depths (−0.01, −0.03, −0.05, −0.07, −0.10,
21 −0.20, −0.40, and −0.60 m): one inlet for the carrier gas, i.e., synthetic dry air (20.5 % O₂ in
22 N₂, with approx. 20-30 ppmv water vapor; Air Liquide, Germany), one sample air outlet, and
23 one duct for a soil temperature (T_s) sensor (type K thermocouple, Greisinger electronic
24 GmbH, Regenstauf, Germany; precision: 0.1°C). An additional fourth port at depths −0.01, −
25 0.03, −0.05, −0.10, −0.20, and −0.60 m was used for the measurement of soil volumetric water
26 content (θ) (EC-5, Decagon Devices, USA; precision: 0.02 m³ m⁻³).

27 At each depth inside the column a 0.15 m long piece of microporous polypropylene tubing
28 (Accurel® PP V8/2HF, Membrana GmbH, Germany; 0.155 cm wall thickness, 0.55 cm i.d.,
29 0.86 cm o.d.) was connected to the gas inlet and outlet port. The tubing offers the two
30 advantages of being gas-permeable (pore size of 0.2 μm) and exhibiting strong hydrophobic

1 properties to prevent liquid water from intruding into the tubing. It allows sampling of soil
2 water vapor and, hence, the determination of the isotope composition of soil liquid water
3 (δ_{Sliq}) in a non-destructive manner considering thermodynamic equilibrium between liquid
4 and vapor phases as detailed by Rothfuss et al. (2013).

5 **2.3 Internal isotope standards**

6 Two internal standards (“st1” and “st2”) were prepared using the same procedure as described
7 by Rothfuss et al. (2013). Two closed acrylic glass vessels (0.122 m i.d., 0.22 m height), in
8 each of which a 0.15 meter long piece of tubing as well as a type K thermocouple were
9 installed, were filled with FH31 sand (porosity = $0.34 \text{ m}^3 \text{ m}^{-3}$, dry bulk density = 1.69 g cm^3 ,
10 particle size distribution: 10% (>0.5 mm), 72% (0.25-0.5 mm), and 18% (<0.25 mm)) (Merz
11 et al., 2014; Stingaciu et al., 2009). Each vessel was saturated with water of two different
12 isotope compositions: $\delta^2\text{H}_{\text{st1}} = -53.51 (\pm 0.10) \text{ ‰}$, $\delta^{18}\text{O}_{\text{st1}} = -8.18 (\pm 0.06) \text{ ‰}$ and $\delta^2\text{H}_{\text{st2}} =$
13 $+15.56 (\pm 0.12) \text{ ‰}$, $\delta^{18}\text{O}_{\text{st2}} = +8.37 (\pm 0.04) \text{ ‰}$. Soil water vapor from each vessel was
14 sampled eight times per day for 30 min during the whole experiment.

15 **2.4 Atmospheric measurements**

16 Laboratory air was sampled passively with a 1/8” three meter-long stainless steel tubing at 2
17 m above the sand surface for isotope analysis of water vapor (δ_a). Air relative humidity (rh)
18 and temperature (T_a) were monitored at the same height with a combined rh and T_a sensor
19 (RFT-2, UMS GmbH, Germany; precision for rh and T_a were 2 % and 0.1°C , respectively).
20 Vapor pressure deficit (vpd) was calculated from rh and T_a data using the Magnus-Tetens
21 formula (Murray, 1967) for saturated vapor pressure. The laboratory was air-conditioned and
22 ventilated with seven axial fans (ETRI 148VK0281, 117 l s^{-1} airflow, ETRI/Rosenberg, USA)
23 positioned at 1.80 m height above the sand surface.

24 **2.5 Sampling protocol and applied isotopic calibrations**

25 The column was filled in a single step with FH31 sand and carefully shaken in order to reach
26 a dry bulk density close to *in situ* field conditions. The sand was then slowly saturated from
27 the bottom from an external water tank filled with st1 water on December 2, 2013. After
28 saturation, the column was disconnected and sealed at the bottom using the two-way manual

1 valve. It was finally installed on a balance (Miras 2 – 60EDL, Sartorius, USA), and let to
2 evaporate for a period of 290 days in a ventilated laboratory.

3 δ_{Sliq} was determined in a sequential manner at each available depth once a day following the
4 method developed by Rothfuss et al. (2013) (Fig. 1b). Dry synthetic air at a rate of 50 ml min⁻¹
5 from a mass flow controller (EL-FLOW Analog, Bronkhorst High Tech, Ruurlo, The
6 Netherlands) was directed to the permeable tubing for 30 minutes at each depth. The sampled
7 soil water vapor was diluted with dry synthetic air provided by a second mass flow controller
8 of the same type. This allowed (i) reaching a water vapor mixing ratio ranging between
9 17,000 and 23,000 ppmv (where L1102-i isotope measurements are most precise) and (ii)
10 generating an excess flow downstream of the laser analyser. By doing this, any contamination
11 of sample air with ambient air would be avoided. The excess flow was measured with a
12 digital flow meter (ADM3000, Agilent Technologies, Santa Clara, CA, USA). The last 100
13 observations (corresponding to approx. 10 minutes) at steady state (standard deviations <0.70
14 ‰ and <0.20 ‰ for $\delta^2\text{H}$ and $\delta^{18}\text{O}$, respectively) were used to calculate the raw isotope
15 compositions of soil water vapor (δ_{Svap}). The latter was corrected for the water vapor mixing
16 ratio dependence of the laser analyzer readings with 17,000 ppmv as reference level.
17 Measurements that did not fulfil the above mentioned conditions for $\delta^2\text{H}$ and $\delta^{18}\text{O}$ standard
18 deviations were not taken into account. Finally, these corrected values were used to infer the
19 corresponding δ_{Sliq} at the measured T_s (Eq. (1) and (2); taken from Rothfuss et al., 2013):

$$20 \quad \delta^2\text{H}_{\text{Sliq}} = 104.96 - 1.0342 \cdot T_s + 1.0724 \cdot \delta^2\text{H}_{\text{Svap}} \quad (1)$$

$$21 \quad \delta^{18}\text{O}_{\text{Sliq}} = 11.45 - 0.0795 \cdot T_s + 1.0012 \cdot \delta^{18}\text{O}_{\text{Svap}} \quad (2)$$

22 The isotope composition of laboratory water vapor (δ_a) was measured eight times a day. δ_a ,
23 δ_{Svap} , and δ_{Sliq} values were finally corrected for laser instrument drift with time, using the
24 isotope compositions of the two water standards, δ_{st1} and δ_{st2} .

25 Water vapor of the ambient air, of both standards, and from the different tubing sections in the
26 soil column were sampled sequentially in the following order: soil (0.60 m) – soil (0.40 m) –
27 atmosphere – st1 – st2 – soil (0.20 m) – soil (0.10 m) – atmosphere – st1 – st2 – soil (0.07 m)
28 – soil (0.05 m) – atmosphere – st1 – st2 – soil (0.03 m) – soil (0.01 m). Atmosphere water
29 vapor was sampled twice as long (i.e., one hour) as soil water vapor from the
30 column/standards so that each sequence lasted exactly 10 hours and started each day at the

1 same time. The remaining 14 hours were used for additional standard and atmosphere water
 2 vapor measurements (i.e., on five occasions each).

3 **2.6 Irrigation event**

4 On Day of Experiment (DoE) 290 at 09:30 the sand surface was irrigated with 70 mm of st1
 5 water. This was achieved over one hour in order to avoid oversaturation of the sand and avoid
 6 preferential pathways that would have affected the evaporation rate. For this, a 2 L
 7 polyethylene bottle was used. Its bottom was perforated with a set of 17 holes of 5 mm
 8 diameter and its cap with a single hole through which a PTFE bulkhead union tube fitting
 9 (Swagelok, USA) was installed. The bulkhead fitting was connected to a two-way needle
 10 valve (Swagelok, USA). Opening/closing the valve controlled the flow rate at which air
 11 entered the bottle headspace, which in turn controlled the irrigation flow rate.

12 To better observe the dynamics directly following the irrigation event, water vapor was
 13 sampled at a higher rate, i.e., 1, 3, 4, 5, 6, 9, 11, and 11 times per day at -0.60 , -0.40 , -0.20 , $-$
 14 0.10 , -0.07 , -0.05 , -0.03 , and -0.01 m. Water vapor from both standards was sampled twice a
 15 day. The experiment was terminated after 299 days on September 26th, 2014.

16 **2.7 Evaporation lines (Craig and Gordon model, 1965)**

17 Gat et al. (1971) proposed an expression based on the model of Craig and Gordon (1965) for
 18 the slope of the so-called “evaporation line” (S_{Ev}) which quantifies the relative change in δ^2H
 19 and $\delta^{18}O$ in a water body undergoing evaporation:

$$20 \quad S_{Ev} = \frac{\Delta(\delta^2H_{Sliq})}{\Delta(\delta^{18}O_{Sliq})} = \frac{rh \cdot (\delta^2H_a - \delta^2H_{Sliq_ini}) + \varepsilon_{eq}^{2H} + \Delta\varepsilon^{2H}}{rh \cdot (\delta^{18}O_a - \delta^{18}O_{Sliq_ini}) + \varepsilon_{eq}^{18o} + \Delta\varepsilon^{18o}} \quad (3)$$

21 where $\Delta\varepsilon^{2H}$ (resp. $\Delta\varepsilon^{18o}$) is the so-called “isotope kinetic effect” associated with $^1H^2H^{16}O$
 22 (resp. $^1H_2^{18}O$) vapor transport:

$$23 \quad \Delta\varepsilon^{2H} = (1 - rh) \cdot \varepsilon_K^{2H} \quad (4a)$$

$$24 \quad \Delta\varepsilon^{18o} = (1 - rh) \cdot \varepsilon_K^{18o} \quad (4b)$$

25 $\delta^2H_{Sliq_ini}$ (resp. $\delta^{18}O_{Sliq_ini}$) is the initial soil liquid δ^2H (resp. $\delta^{18}O$), i.e., prior removal of
 26 water vapor by fractionating evaporation. ε_{eq}^{2H} (resp. ε_{eq}^{18o}) and ε_K^{2H} (resp. ε_K^{18o}) are the

1 equilibrium and kinetic $^1\text{H}^2\text{H}^{16}\text{O}$ (resp. $^1\text{H}_2^{18}\text{O}$) enrichments. $\varepsilon_{\text{eq}}^{2\text{H}}$ (resp. $\varepsilon_{\text{eq}}^{18\text{o}}$) is defined by
2 the deviation from unity of the ratio between water and $^1\text{H}^2\text{H}^{16}\text{O}$ (resp. $^1\text{H}_2^{18}\text{O}$) saturated
3 vapor pressures and can be calculated using the empirical closed-form equations proposed by,
4 e.g., Majoube (1971). $\varepsilon_{\text{K}}^{2\text{H}}$ (resp. $\varepsilon_{\text{K}}^{18\text{o}}$) is defined as the deviation from unity of the ratio
5 between the resistance associated with the transport of $^1\text{H}^2\text{H}^{16}\text{O}$ (resp. $^1\text{H}_2^{18}\text{O}$) vapor in the
6 boundary air layer above the evaporating surface and that of water vapor. By assuming that (i)
7 turbulent transport is a non-fractionating process and (ii) resistance associated with molecular
8 diffusion of $^1\text{H}^2\text{H}^{16}\text{O}$ (resp. $^1\text{H}_2^{18}\text{O}$) vapor is inversely proportional to the n^{th} power of the
9 corresponding diffusivity ($D^{2\text{H}}$, resp. $D^{18\text{o}}$), Merlivat and Coantic (1975) proposed the
10 following expressions:

$$11 \quad \varepsilon_{\text{K}}^{2\text{H}} = \left(\frac{D}{D^{2\text{H}}} \right)^n - 1 = (1.0251)^n - 1 \quad (5a)$$

$$12 \quad \varepsilon_{\text{K}}^{18\text{o}} = \left(\frac{D}{D^{18\text{o}}} \right)^n - 1 = (1.0285)^n - 1 \quad (5b)$$

13 The exponent n accounts for the aerodynamic regime above the liquid–vapor interface (i.e.,
14 where the relative humidity is 100%) and ranges from $n_{\text{a}} = 0.5$ (fully turbulent, i.e.,
15 atmosphere-controlled conditions) to $n_{\text{s}} = 1$ (fully diffusive, i.e., soil-controlled conditions)
16 with a value of $\frac{2}{3}$ corresponding to laminar flow conditions (Dongmann et al., 1974,
17 Brutsaert, 1975). In the present study, values for ratios of diffusivities ($D/D^{2\text{H}}$ and $D/D^{18\text{o}}$)
18 were taken from Merlivat (1978) and n was considered as a function of soil water content as
19 proposed by Mathieu and Bariac (1996):

$$20 \quad n = \frac{(\theta_{\text{surf}} - \theta_{\text{res}}) \cdot n_{\text{a}} + (\theta_{\text{sat}} - \theta_{\text{res}}) \cdot n_{\text{s}}}{\theta_{\text{sat}} - \theta_{\text{res}}} \quad (6)$$

21 with θ_{res} , θ_{sat} , and θ_{surf} the residual, saturated and surface soil water contents ($\text{m}^3 \text{m}^{-3}$).

22 Note that Equation (3) contrasts with the expression for the slope characterizing equilibrium
23 processes (e.g., precipitation formation) and therefore strictly temperature-dependant (i.e.,
24 $S_{\text{eq}} = \varepsilon_{\text{eq}}^{2\text{H}} / \varepsilon_{\text{eq}}^{18\text{o}}$). While S_{eq} might range for instance from 7.99 to 8.94 (for temperatures
25 spanning between 5 and 30°C), a much wider spread in S_{Ev} values is possible and has been

1 measured between 2 and 6 (Barnes and Allison, 1988, Brunel et al., 1995, DePaolo et al.,
2 2004).

3 **3 Results**

4 **3.1 Example of a measuring sequence**

5 Figure 2 shows exemplarily the measuring sequence for DoE 150. Soil and standards water
6 vapor mixing ratios were stable and ranged from 17,200 to 18,200 ppmv during the last 10
7 minutes of each sampling period (Fig. 2a). δ_{Svap} was within the range spanned by δ_{st1vap} and
8 δ_{st2vap} for both ^2H and ^{18}O (Fig. 2b). On DoE 150, the soil surface was sufficiently dry so that
9 atmospheric invasion of water vapor had started to significantly influence the δ_{Svap} of the
10 upper soil layers. Therefore, δ_{Svap} measured at -0.01 m was lower than at -0.03 m for both ^2H
11 and ^{18}O , but less pronounced for ^2H .

12 **3.2 Time courses of air temperature, relative humidity and atmospheric $\delta^2\text{H}$** 13 **and $\delta^{18}\text{O}$**

14 During the experiment, the laboratory air temperature ranged from 15.6 to 22.5 °C (average:
15 18.7 ± 1.5 °C, Fig. 3a) and the relative humidity from 19 to 69 % (average: 40 % \pm 0.08 %,
16 Fig. 3a). Lower values of δ_a were observed from DoE 0 to 125 at lower air temperatures,
17 whereas higher values occurred after DoE 125 at higher air temperatures (Fig. 3b).

18 **3.3 Evolution of soil water content, temperature, evaporation flux, and δ_{Svap}** 19 **from DoE 0-290**

20 The soil temperature ranged from 16.2 to 22.3 °C (average: 18.6 ± 1.3 °C, data not shown)
21 and closely followed that in the air, i.e., differences between daily mean soil and air
22 temperatures ranged from -0.2 to 0.2 °C during the experiment. Following the saturation of
23 the column, a strong decrease in water content was observed in the upper 10 cm, whereas
24 after 287 days the sand was still saturated at -0.60 m (Fig. 4a). Figure 4b shows the time
25 series of evaporation flux normalized by the vapor pressure deficit in the laboratory air
26 (Ev/vpd , expressed in $\text{mm day}^{-1} \text{ kPa}^{-1}$). Ev/vpd ratio was high at the beginning of the
27 experiment, i.e., ranged from 2.44 to 3.22 $\text{mm d}^{-1} \text{ kPa}^{-1}$ during the first two experimental
28 days. After DoE 180 and until the soil was irrigated, Ev/vpd stabilized to a mean value of 0.03
29 (± 0.02) $\text{mm d}^{-1} \text{ kPa}^{-1}$.

1 Due to fractionating evaporation flux, the δ_{Svap} of the topmost layer (-0.01 m) increased
 2 instantaneously (i.e., from DoE 0 onward) from the equilibrium δ_{Svap} value with the input
 3 water (-17.3 ‰ and -132.3 ‰ for ^{18}O and ^2H , respectively, at 16.5°C , Fig. 4c and d).
 4 Through back-diffusion of the excess heavy stable isotopologues from the evaporation front,
 5 δ_{Svap} measured at depths -0.03 , -0.05 , -0.07 , -0.10 , and -0.20 m departed from that same
 6 equilibrium value after 2, 3, 10, 25, and 92 days of the experiment, respectively. On the other
 7 hand, δ_{Svap} of the layers -0.40 and -0.60 m were constant over the entire duration of the
 8 experiment. Until DoE 65, the δ_{Svap} of the first 10 cm increased. From DoE 65 to 113 δ_{Svap}
 9 reached an overall stable value in the top layers -0.01 m ($\delta^2\text{H}_{\text{Svap}} = 4.82 \pm 2.06$ ‰; $\delta^{18}\text{O}_{\text{Svap}} =$
 10 11.72 ± 0.67 ‰) and -0.03 m ($\delta^2\text{H}_{\text{Svap}} = 5.61 \pm 3.14$ ‰; $\delta^{18}\text{O}_{\text{Svap}} = 10.41 \pm 0.81$ ‰), whereas
 11 δ_{Svap} measured at depths -0.05 , -0.07 , and -0.10 m still progressively increased; from DoE 72
 12 onward, δ_{Svap} at -0.20 m started to increase. $\delta^2\text{H}_{\text{Svap}}$ and $\delta^{18}\text{O}_{\text{Svap}}$ values started to decrease
 13 after about DoE 113 and DoE 155, respectively. $\delta^2\text{H}_{\text{Svap}}$ at -0.01 , -0.03 , and -0.07 m on the
 14 one hand and $\delta^{18}\text{O}_{\text{Svap}}$ at -0.01 , -0.03 , and -0.07 m on the other followed similar evolutions
 15 with maximum values measured below the surface down to -0.05 m.

16 **3.4 Evolution of soil water content, temperature, evaporation flux, and δ_{Svap}** 17 **from DoE 290 to 299**

18 The layers -0.01 , -0.03 , -0.05 , -0.10 , and -0.20 m showed increases in θ of 0.31, 0.22, 0.30,
 19 0.23, and $0.16 \text{ m}^3 \text{ m}^{-3}$ following irrigation, whereas θ at -0.60 m remained constant (Fig. 4e).
 20 $\theta_{-0.01\text{m}}$ and $\theta_{-0.03\text{m}}$ rapidly decreased down to values of 0.12 and $0.13 \text{ m}^3 \text{ m}^{-3}$. Note that when
 21 $\theta_{-0.01\text{m}}$ and $\theta_{-0.03\text{m}}$ reached these values prior to irrigation, the evaporation rate was similar
 22 (i.e., $Ev/vpd = 0.65 (\pm 0.12) \text{ mm d}^{-1}$, Fig. 4f).

23 Immediately after irrigation and for both isotopologues, δ_{Svap} at -0.01 , -0.03 , and -0.05 m
 24 was reset to a value close to that in equilibrium with st1 water (i.e., -17.8 ‰ and -132.0 ‰
 25 for ^{18}O and ^2H , respectively, at 21.8 °C soil temperature, Fig. 4g and h). At -0.07 m, δ_{Svap}
 26 reached the above mentioned equilibrium values after about 3.5 days. δ_{Svap} at -0.20 m evolved
 27 in a similar way, whereas at -0.10 m the equilibrium values were reached after six hours.
 28 Finally, δ_{Svap} at -0.40 and -0.60 m and for both isotopologues were not affected by the water
 29 addition, which was consistent with the observed θ changes.

1 **3.5 Evolution of soil temperature, water content, and δ_{Sliq} profiles**

2 In Figure 5, T_s , θ , and δ_{Sliq} profiles for both isotopologues are plotted in three different panels,
3 from DoE 0 to 100 (Fig. 5a-d, top panels), from DoE 101 to 287 (Fig. 5e-h, center panels),
4 and from DoE 288 to 299 (Fig. 5i-l, bottom panels). The represented profiles were obtained
5 from a linear interpolation of the times series of each variable. Thus, since the measuring
6 sequence started each day at 08:00 and ended at 18:00, the depicted profiles are centered on
7 13:00.

8 Even if the soil temperature fluctuated during the course of the experiment, quasi-isothermal
9 conditions were fulfilled at a given date, as the column was not isolated from its surroundings.
10 On average, T_s only varied by 0.2 °C around the profile mean temperature at a given date.
11 The δ_{Sliq} profiles showed a typical exponential shape from DoE 0 to approx. 100. Around DoE
12 100, when θ at -0.01 m reached a value of $0.090 \text{ m}^3 \text{ m}^{-3}$ (i.e., significantly greater than the
13 sand residual water content $\theta = 0.035 \text{ m}^3 \text{ m}^{-3}$, determined by Merz et al. (2014)), the maximal
14 δ_{Sliq} values were no longer observed at the surface and atmosphere water vapor started
15 invading the first centimeter of soil. Note that this happened slightly faster for $^1\text{H}^2\text{H}^{16}\text{O}$ than
16 for $^1\text{H}_2^{18}\text{O}$. On DoE 290, when the column was irrigated, the isotope profiles were partly reset
17 to their initial state, i.e., constant over depth and close to -53.5 and -8.2 ‰ for $^1\text{H}^2\text{H}^{16}\text{O}$ and
18 $^1\text{H}_2^{18}\text{O}$, respectively, with the exception of still enriched values at -0.07 m.

19 **3.6 $\delta^2\text{H}$ - $\delta^{18}\text{O}$ relationships in soil water and atmosphere water vapor**

20 Each plot of Figure 6 represents data of 50 consecutive days of the experiment. Laboratory
21 atmosphere water vapor $\delta^2\text{H}$ and $\delta^{18}\text{O}$ (gray symbols) were linearly correlated (linear
22 regression relationships in gray dotted lines) during the entire experiment (R^2 ranging
23 between 0.74 and 0.90, F-statistic p-value < 0.01), with the exception of the period DoE 125-
24 155 ($R^2 = 0.31$, $p < 0.001$), when atmospheric water vapour $\delta^2\text{H}$ was remarkably high in the
25 laboratory (Fig. 6c and d).

26 The linear regression slopes (LRS) between $\delta^2\text{H}_a$ and $\delta^{18}\text{O}_a$ ranged from 6.20 (DoE 50-100, p
27 < 0.01) to 8.29 (DoE 0-50, gray dotted line, $p < 0.001$). These values were significantly lower
28 than S_{eq} , the calculated ratio between the liquid-vapor equilibrium fractionations of $^1\text{H}^2\text{H}^{16}\text{O}$
29 and $^1\text{H}_2^{18}\text{O}$ (Majoube, 1971) that characterizes meteoric water bodies, which should have
30 ranged from 8.41 to 8.92 at the measured monthly mean atmosphere temperatures
31 (Forschungszentrum Jülich wheater station, $6^\circ 24' 34''$ E, $50^\circ 54' 36''$ N, 91 m.a.s.l.). Therefore,

1 it can be deduced that the laboratory air moisture was partly resulting from column
2 evaporation, typically leading to a $\delta^2\text{H}-\delta^{18}\text{O}$ regression slope of lower than eight. This also
3 highlights the particular experimental conditions in the laboratory, where other sources of
4 water vapour (e.g., by opening the laboratory door) might have influenced the isotope
5 compositions of the air.

6 Considering all soil depths, the $\delta^2\text{H}_{\text{Sliq}}-\delta^{18}\text{O}_{\text{Sliq}}$ LRS increased from 2.96 to 4.86 over the
7 course of the experiment (with $R^2 > 0.89$, $p < 0.001$). These values were much lower than that
8 of the slope of the Global Meteoric Water Line (GMWL, i.e., slope=8) also represented in
9 Figure 6. However, Figure 6 highlights the fact that in the upper three layers (-0.01, -0.03,
10 and -0.05 m) $\delta^2\text{H}_{\text{Sliq}}-\delta^{18}\text{O}_{\text{Sliq}}$ LRS followed a significantly different evolution as the soil dried
11 out. Figure 7 shows average $\delta^2\text{H}-\delta^{18}\text{O}$ LRS calculated for time intervals of ten consecutive
12 days for the atmosphere (gray line), the three upper layers (colored solid lines), and the
13 remaining deeper layers (-0.07, -0.10, -0.20, -0.40, and -0.60 m, black dotted line). While
14 both $\delta^2\text{H}-\delta^{18}\text{O}$ LRS in the atmosphere and in the first three depths fluctuated during the
15 experiment, the LRS of the combined remaining deeper layers varied only little between 3.07
16 and 4.49 (average = 3.78 ± 0.54). From DoE 150, $\delta^2\text{H}-\delta^{18}\text{O}$ LRS of the atmosphere and at -
17 0.01, -0.03, and -0.05 m were linearly correlated ($R^2 = 0.73, 0.48, \text{ and } 0.42$, with $p < 0.001, <$
18 0.01 , and < 0.05 , respectively), whereas they were not correlated before DoE 125,
19 demonstrating again the increasing influence of the atmosphere (atmosphere invasion) on the
20 soil surface layer as the EF receded in the soil. Note the negative $\delta^2\text{H}_a-\delta^{18}\text{O}_a$ LRS ($R^2 = 0.26$,
21 $p < 0.001$) observed between DoE 125 and 150, due to remarkably high atmosphere vapor
22 $\delta^2\text{H}$ measured in the laboratory.

23

24 **4 Discussion**

25 **4.1 Long term reliability of the method**

26 The method proved to be reliable in the long term as the tubing sections positioned at -0.60
27 and -0.40 m (i.e., where the sand was saturated or close to saturation during the entire
28 experiment) remained watertight even after 299 days. As demonstrated by Rothfuss et al.
29 (2013), (i) the length of the gas-permeable tubing, (ii) the low synthetic dry air flow rate, and
30 (iii) the daily measurement frequency allowed removing soil water vapor which remained
31 under thermodynamic equilibrium with the soil moisture. Moreover, this was also true for the

1 upper soil layers even at low soil water content: steady values for water vapor mixing ratio
2 and isotope compositions were always reached during sampling throughout the experiment.
3 Finally, our method enabled inferring the isotope composition of tightly bound water at the
4 surface. This would be observable by the traditional vacuum distillation method with certainly
5 a lower vertical resolution due to low moisture content. As also pointed out by Rothfuss et al.
6 (2013), it can be assumed that the sand properties did not cause any fractionation of pore
7 water ^2H and ^{18}O . In contrast, this could not be the case in certain soils with high cation
8 exchange capacity (CEC) as originally described by Sofer and Gat (1972) and recently
9 investigated by Oerter et al. (2014).

10 **4.2 Locating the evaporation front depth from soil water $\delta^2\text{H}$ and $\delta^{18}\text{O}$ profiles**

11 From Figure 4b no distinct characteristic evaporation stages, i.e., stages I and II referring to
12 atmosphere-controlled and soil-controlled evaporation phases, respectively, could be
13 identified. The opposite was observed by Merz et al. (2014), who conducted an evaporation
14 study using the same sand. This indicates greater wind velocity in the air layer above the soil
15 column due to the laboratory ventilation. For higher wind velocities, the boundary layer above
16 the drying medium is thinner and the transfer resistance for vapor transfer lower than for
17 lower wind velocities. But, for thinner boundary layers, the evaporation rates depends
18 stronger on the spatial configuration of the vapor field above the partially wet evaporating
19 surface. This makes that the evaporation rate decreases and the transfer resistance in the
20 boundary layer increases more in relative terms with decreasing water content of the
21 evaporation surface for higher than for lower wind velocities (Shahraeeni et al., 2012).

22 Locating the EF in the soil is of importance for evapotranspiration partitioning purposes: from
23 the soil water isotope composition at the EF, it is possible to calculate the evaporation flux
24 isotope composition using the Craig and Gordon formula (Craig and Gordon, 1965). For a
25 uniform isotope diffusion coefficient distribution in the liquid phase, an exponential decrease
26 of the isotope composition gradient with depth is expected. However, when evaporation and
27 thus accumulation of isotopologues occur in a soil layer between two given observation
28 points, then the isotope gradient between these two points is smaller than the gradient deeper
29 in the profile. Therefore we can consider the time when the isotope composition gradient is no
30 longer the largest between these two upper observation depths as the time when the EF moves
31 into the soil layer below.

1 Figure 8a and b display the evolutions of the isotope compositions gradients $d(\delta^{18}O_s)/dz$ and
2 $d(\delta^2H_s)/dz$ calculated between two consecutive observation points in the soil (i.e., between
3 -0.01 and -0.03 m in brown solid line, between -0.03 and -0.05 m in red solid line, etc.).
4 Figure 8c translates these isotope gradients in terms of EF depths ($z^{18}O_{EF}$ and z^2H_{EF} ,
5 respectively). Each day, the maximum $d(\delta^{18}O_s)/dz$ and $d(\delta^2H_s)/dz$ define the layer where
6 evaporation occurs, e.g., when $d(\delta^{18}O_s)/dz$ is maximal between -0.01 and -0.03 m on a given
7 DoE, $z^{18}O_{EF}$ is estimated to be greater than -0.01 m and is assigned the value of 0 m.
8 When $d(\delta^{18}O_s)/dz$ is maximal between -0.03 and -0.05 m on a given DoE, $z^{18}O_{EF}$ is
9 estimated to range between -0.01 and -0.03 m and is assigned the value -0.02 m. From
10 both $d(\delta^{18}O_s)/dz$ and $d(\delta^2H_s)/dz$, a similar evolution of the depth of the evaporation front
11 was derived despite the fact that δ^2H_{Sliq} and $\delta^{18}O_{Sliq}$ time courses were different and showed
12 maxima at different times. It was inferred that after 290 days under the prevailing laboratory
13 air temperature, moisture, and aerodynamic conditions, and given the specific hydraulic
14 properties of the sand, the EF had moved down to an approximate depth of -0.06 m.

15 **4.3 Testing the Craig and Gordon (1965) relationship with isotope data**

16 For each period of ten consecutive days the minimum measured δ^2H_{Sliq} and $\delta^{18}O_{Sliq}$ provided
17 $\delta^2H_{Sliq_ini}$ and $\delta^{18}O_{Sliq_ini}$ in Equation (3). δ^2H_a and $\delta^{18}O_a$ were obtained from the mean values
18 of their respective times series. Mean soil surface water content (θ_{surf}) measured in the layer
19 above the EF (as identified in section 4.2) provided the n parameter in Equation (6) and
20 ultimately ε_K^{2H} and ε_K^{18O} (Eq. (5a) and (5b)). ε_{eq}^{2H} and ε_{eq}^{18O} were calculated from Majoube (1971)
21 at the mean soil temperature measured at z_{EF} . Relative humidity was normalized to the soil
22 temperature measured at the EF. Finally, standard error for S_{Ev} was obtained using an
23 extension of the formula proposed by Phillips and Gregg (2001) and detailed by Rothfuss et
24 al. (2010). For this, standard errors associated with the determination of the variables in
25 Equation (3) were taken equal to their measured standard deviations for each time period.
26 Standard errors for the parameters θ_{res} and θ_{sat} were set arbitrarily to $0.01 \text{ m}^3 \text{ m}^{-3}$ and for the
27 diffusivity ratios D/D^{2H} and D/D^{18O} to zero (i.e., no uncertainty about their value was taken
28 into account, although debatable, e.g., Cappa et al., 2003).

29 Figure 9a shows the comparison between time courses of S_{Ev} and $\delta^2H_{Sliq}-\delta^{18}O_{Sliq}$ LRS
30 computed with data below the EF. Both ranged between 2.9 and 4.8, i.e., within the range of

1 reported values (e.g., Barnes and Allison, 1988, Brunel et al., 1995, DePaolo et al., 2004).
2 Note that both observed and simulated slopes' values increased over time, even though the
3 boundary air layer above the EF gradually thickened as the soil dried out. The opposite was
4 observed by e.g., Barnes and Allison (1983), who simulated isotopic profiles at steady state
5 with constant relative humidity. In the present study however the atmosphere relative
6 humidity gradually increased which in turn decreased the kinetic effects associated with
7 $^1\text{H}^2\text{H}^{16}\text{O}$ and $^1\text{H}_2^{18}\text{O}$ vapour transports and thus increased slopes over time. The general
8 observed trend was very well reproduced by the model between DoE 30 and 150 (Nash and
9 Sutcliffe Efficiency - NSE = 0.92; Nash and Sutcliffe, 1970), whereas S_{Ev} departed from data
10 from DoE 150 onwards (NSE < 0). Overall, the Craig and Gordon (1965) model could
11 explain about 62 % of the data variability with a Root Mean Square Error (RMSE) of 0.58
12 (and 76 % when data from the period DoE 0-10 is left out, p-value < 0.001, RMSE = 0.52). At
13 the beginning of the experiment (DoE 0-20), simulated values were greater than computed
14 $\delta^2\text{H}-\delta^{18}\text{O}$ LRS, even when taking into account the high S_{Ev} standard errors due to fast
15 changing θ_{surf} (Phillips and Gregg, 2001). Although S_{Ev} was equal to 3.8 for the period DoE 0-
16 10, $\delta^2\text{H}-\delta^{18}\text{O}$ LRS had already reached down a value of 2.9, meaning that the EF should have
17 been no longer at the surface (i.e., between the surface and 0.01 m depth) leading to greater n,
18 therefore lower slope value.

19 After DoE 150 and until DoE 290 when evaporation flux was lower than 0.40 mm d⁻¹,
20 difference between model and data progressively increased. For a better model-to-data fit, the
21 $^1\text{H}^2\text{H}^{16}\text{O}$ and $^1\text{H}_2^{18}\text{O}$ kinetic effects should decrease, through either (i) decrease of ε_{K} (i.e.,
22 decrease of n), which is from a theoretical point of view counter-intuitive and e.g., contradicts
23 the formulation of Mathieu and Bariac (1996) or (ii) decrease of term $(1 - rh)$, or else (iii) a
24 combination of (i) and (ii). In another laboratory study where $\delta^{18}\text{O}$ of water in bare soil
25 columns was measured destructively and $\delta^{18}\text{O}$ of evaporation was estimated from cryoscopic
26 trapping of water vapour at the outlet of the columns' headspaces, Braud et al. (2009a and b)
27 could capture $\varepsilon_{\text{K}}^{18\text{o}}$ dynamics by inverse modelling. In their case, $\varepsilon_{\text{K}}^{18\text{o}}$ generally reached values
28 close to $\varepsilon_{\text{K}}^{18\text{o}} = 18.9\text{‰}$ corresponding to laminar conditions above the liquid-vapor interface (n
29 = 2/3). They however determined at the end of their experiments, when the soil surface dry
30 layer thickened and soil surface relative humidity was significantly lower than 100%, values
31 lower than reported in the literature (i.e., $\varepsilon_{\text{K}}^{18\text{o}} < 14.1\text{‰}$). These results were partly explained
32 by the particular experimental conditions leading to uncertainties in characterizing

1 evaporation isotope compositions when the dry soil surface layer was the most developed.
2 Nevertheless, the same observation could be made in the present study while having a
3 different soil texture (silt loam *versus* quartz sand) and noticeable different atmospheric
4 conditions (“free” laboratory atmosphere *versus* sealed headspace circulated with dry air).
5 Figure 9c displays the evolution of ε_K^{2H} (resp. ε_K^{18O}) that provided the best fit with data (NSE =
6 0.99) through fitting of the n parameter (shown Figure 9b) instead of calculating it with
7 Equation (6). In this scenario, n decreased from one to 0.59, with a mean value of 0.96 ± 0.03
8 during the period DoE 0-150.

9 Instead of changing the value of n over time (and therefore those of ε_K^{2H} and ε_K^{18O}), another
10 possibility is to consider that after some time the relative humidity at the EF (rh_{EF}) was
11 different from 100%, although the EF was still at thermodynamic equilibrium. In that case
12 kinetic effects would have depended on the difference ($rh_{EF} - rh$) instead of $(1 - rh)$. Figure
13 9b shows the rh_{EF} time course that provided the best model-to-data fit (NSE = 0.92), when
14 ε_K^{2H} and ε_K^{18O} were calculated (Eq. (5a-5b-6)). In this second scenario, rh_{EF} decreased from 100
15 to 81 % with a mean value of 99.5 ± 0.03 % for the period DoE 0-150, i.e., in a similar
16 fashion than fitted n values obtained in the 1st scenario. These values were significantly lower
17 than what is calculated with Kelvin’s Equation linking rh_{EF} with soil water tension at the EF
18 in the case of liquid-vapor equilibrium, which for the soil retention properties (Merz et al.,
19 2014) would range between 100 and 99.6 %. In a third scenario one could consider a
20 combined decrease of n and rh_{EF} to smaller extents, for which there are no unique solutions at
21 each time step. In any case, only decreasing kinetic effects could provide a better model-to-
22 data fit. In the present study, information on δ^{2H} and δ^{18O} of the evaporation flux was missing
23 to address uncertainties in the determination of ε_K^{2H} and ε_K^{18O} . The experimental setup would
24 also have gained from the addition of appropriate sensors (e.g., micro-psychrometers) to
25 measure the soil surface relative humidity and especially rh_{EF} , although the dimensions of the
26 column would certainly be a limiting factor. Finally note that S_{Ev} calculations using diffusivity
27 ratios determined by Cappa et al. (2003) lead to lower value of S_{Ev} and less good model-to-
28 data fit. A more in depth investigation of the behavior of S_{Ev} (and isotope composition
29 gradients with depth for that matter) with time could be carried out with detailed numerical
30 simulations using an isotope-enabled SVAT model such as SiSPAT-Isotope.

1 **5 Conclusion**

2 Since the initial work of Zimmermann et al. (1967), water stable isotopologues have proven
3 both theoretically and experimentally to be valuable tools for the study of water flow in the
4 soil and at the soil-atmosphere interface. In this work we present the first application of the
5 method of Rothfuss et al. (2013). This study constitutes also the very first long-term
6 application of the series of newly developed isotopic monitoring systems based on gas-
7 permeable tubing and isotope-specific infrared laser absorption spectroscopy (Herbstritt et al.,
8 2012; Volkmann and Weiler, 2014). Our method proved to be reliable over long time periods
9 and followed quantitatively the progressive isotope enrichment caused by evaporation in an
10 initially saturated soil column. Moreover, it could capture sudden variations following a
11 simulated intense rain event.

12 Simple calculations of isotope compositions' gradients made it possible to evaluate the
13 position of the Evaporation Front and observe how it progressively receded with time in the
14 soil. Confrontation of the model of Craig and Gordon (1965) with data also highlighted
15 uncertainties associated with the determinations of isotope kinetic fractionations and soil
16 relative humidity at the EF when the soil surface dry layer was the most developed and
17 evaporation flux was low.

18 Our method will allow experimentalists to measure and locate the evaporation front in a
19 dynamic and non-destructive manner and to calculate the isotope compositions of the
20 evaporation flux using the model of Craig and Gordon (1965) with much higher time
21 resolution. Provided that the isotope compositions of evapotranspiration and transpiration
22 fluxes are measured or modelled, this method will be especially useful to test hypotheses and
23 improve our understanding of root water uptake processes and the partitioning of
24 evapotranspiration fluxes.

25

26 **Acknowledgements**

27 This study was conducted in the framework of and with means from the Bioeconomy
28 Portfolio Theme of the Helmholtz Association of German Research Centers. The authors
29 would like to thank Ayhan Egmen and Dieter Mans from the IBG Workshop at
30 Forschungszentrum Jülich for designing and building the acrylic glass column and Holger
31 Wissel for his insight and technical support. Special thanks go to the Institute of Meteorology

1 and Climate Research (IMK-IFU), Karlsruhe Institute of Technology, for providing the water
2 isotopic analyzer for this study.
3

1 **References**

- 2 Barnes, C. J., and Allison, G. B.: The Distribution of Deuterium and O-18 in Dry Soils .1.
3 Theory, *J. Hydrol.*, 60, 141-156, doi: 10.1016/0022-1694(83)90018-5, 1983.
- 4 Barnes, C. J., and Allison, G. B.: The Distribution of Deuterium and O-18 in Dry Soils .3.
5 Theory for Non-Isothermal Water-Movement, *J. Hydrol.*, 74, 119-135, doi: 10.1016/0022-
6 1694(84)90144-6, 1984.
- 7 Barnes, C. J., and Allison, G. B.: Tracing of water movement in the unsaturated zone using
8 stable isotopes of hydrogen and oxygen, *J. Hydrol.*, 100, 143–176, doi:10.1016/0022-
9 1694(88)90184-9, 1988
- 10 Barnes, C. J., and Walker, G. R.: The Distribution of Deuterium and O-18 during Unsteady
11 Evaporation from a Dry Soil, *J. Hydrol.*, 112, 55-67, doi: 10.1016/0022-1694(89)90180-7,
12 1989.
- 13 Blasch, K. W., and Bryson, J. R.: Distinguishing sources of ground water recharge by using
14 delta H-2 and delta O-18, *Ground Water*, 45, 294-308, doi: 10.1111/j.1745-
15 6584.2006.00289.x, 2007.
- 16 Braud, I., Bariac, T., Gaudet, J. P., and Vauclin, M.: SiSPAT-Isotope, a coupled heat, water
17 and stable isotope (HDO and (H₂O)-O-18) transport model for bare soil. Part I. Model
18 description and first verifications, *J. Hydrol.*, 309, 277-300, doi:
19 10.1016/j.jhydrol.2004.12.013, 2005.
- 20 Braud, I., Biron, P., Bariac, T., Richard, P., Canale, L., Gaudet, J. P., and Vauclin, M.:
21 Isotopic composition of bare soil evaporated water vapor. Part I: RUBIC IV experimental
22 setup and results, *J. Hydrol.*, 369, 1-16, DOI 10.1016/j.jhydrol.2009.01.034, 2009a.
- 23 Braud, I., Bariac, T., Biron, P., and Vauclin, M.: Isotopic composition of bare soil evaporated
24 water vapor. Part II: Modeling of RUBIC IV experimental results, *J. Hydrol.*, 369, 17-29,
25 DOI 10.1016/j.jhydrol.2009.01.038, 2009b.
- 26 Brunel, J. P., Walker, G. R, and Kennetsmith, A. K.: Field Validation of Isotopic Procedures
27 for Determining Sources of Water Used by Plants in a Semiarid Environment, *J. Hydrol.*, 167,
28 351-368, doi: 10.1016/0022-1694(94)02575-V, 1995.

1 Brutsaert, W.: A theory for local evaporation (or heat transfer) from rough and smooth
2 surfaces at ground level, *Water Resour. Res.*, 11, 543-550, doi: 10.1029/WR011i004p00543,
3 1975.

4 Craig, H.: Isotopic Variations in Meteoric Waters, *Science*, 133, 1702-1703, doi:
5 10.1126/science.133.3465.1702, 1961.

6 Craig, H., and Gordon, L. I.: Deuterium and oxygen 18 variations in the ocean and marine
7 atmosphere, *Stable Isotopes in Oceanographic Studies and Paleotemperatures*, Spoleto, Italy,
8 1965, 9-130, 1965.

9 DePaolo, D. J., Conrad, M. E., Maher, K., and Gee, G. W.: Evaporation effects on oxygen and
10 hydrogen isotopes in deep vadose zone pore fluids at Hanford, Washington, *Vad. Zone. J.*, 3,
11 220-232, doi:10.2113/3.1.220, 2004.

12 Dongmann, G., H. W. Nurnberg, H. Forstel, and Wagener, K.: Enrichment of H₂¹⁸O in
13 Leaves of Transpiring Plants, *Radiat Environ Bioph*, 1, 41-52, doi: 10.1007/Bf01323099,
14 1974.

15 Dubbert, M., Cuntz, M., Piayda, A., Maguás, C., and Werner, C.: Partitioning
16 evapotranspiration – Testing the Craig and Gordon model with field measurements of oxygen
17 isotope ratios of evaporative fluxes, *J. Hydrol.*, 496, 142-153, doi:
18 10.1016/j.jhydrol.2013.05.033, 2013.

19 Gaj, M., Beyer, M., Koeniger, P., Wanke, H., Hamutoko, J., and Himmelsbach, T.: In-situ
20 unsaturated zone stable water isotope (²H and ¹⁸O) measurements in semi-arid environments
21 using tunable off-axis integrated cavity output spectroscopy, *Hydrol. Earth Syst. Sci. Discuss.*
22 12, 6115-6149, doi:10.5194/hessd-12-6115-2015, 2015.

23 Gat, J.: Comments on the Stable Isotope Method in Regional Groundwater Investigations,
24 *Water Resour. Res.*, 7, 980-993, doi: 10.1029/WR007i004p00980, 1971

25 Goldsmith, G.R., Munoz-Villers, L.E., Holwerda, F., McDonnell, J.J., Asbjornsen, H.,
26 Dawson, T.E.: Stable isotopes reveal linkages among ecohydrological processes in a
27 seasonally dry tropical montane cloud forest, *Ecohydrology*, 5, 779-790, doi:
28 10.1002/eco.268, 2011.

29 Gonfiantini, R.: Standards for stable isotope measurements in natural compounds, *Nature*,
30 271, 534-536, doi: 10.1038/271534a0, 1978.

1 Haverd, V., and Cuntz, M.: Soil-Litter-Iso: A one-dimensional model for coupled transport of
2 heat, water and stable isotopes in soil with a litter layer and root extraction, *J. Hydrol.*, 388,
3 438-455, doi: 10.1016/j.jhydrol.2010.05.029, 2010.

4 Herbstritt, B., Gralher, B., and Weiler, M.: Continuous in situ measurements of stable
5 isotopes in liquid water, *Water Resour. Res.*, 48, doi: 10.1029/2011wr011369, 2012.

6 Hu, Z. M., Wen, X. F., Sun, X. M., Li, L. H., Yu, G. R., Lee, X. H., and Li, S. G.: Partitioning
7 of evapotranspiration through oxygen isotopic measurements of water pools and fluxes in a
8 temperate grassland, *J Geophys Res-Biogeo*, 119, 358-371, doi: 10.1002/2013jg002367,
9 2014.

10 Jasechko, S., Sharp, Z. D., Gibson, J. J., Birks, S. J., Yi, Y., and Fawcett, P. J.: Terrestrial
11 water fluxes dominated by transpiration, *Nature*, 496, 347-351, doi: 10.1038/Nature11983,
12 2013.

13 Litaor, M.I.: Review of Soil Solution Samplers. *Water Resour. Res.*, 24, 727-733, doi:
14 10.1029/Wr024i005p00727, 1988

15 Liu, Z. F., Bowen, G. J., and Welker, J. M.: Atmospheric circulation is reflected in
16 precipitation isotope gradients over the conterminous United States, *J. Geophys. Res.-Atmos.*,
17 115, doi: 10.1029/2010jd014175, 2010.

18 Merlivat, L.: Molecular Diffusivities of H₂¹⁶O, HD¹⁶O, and H₂¹⁸O in Gases, *J. Chem.*
19 *Phys.*, doi: 10.1063/1.436884, 1978

20 Merlivat, L., and Coantic, M.: Study of Mass-Transfer at Air-Water-Interface by an Isotopic
21 Method, *J. Geophys. Res.-Oc. Atm.*, 80, 3455-3464, doi: 10.1029/Jc080i024p03455, 1975

22 Majoube, M.: Oxygen-18 and Deuterium Fractionation between Water and Steam, *J. Chim.*
23 *Phys. Phys.-Chim. Biol.*, 68, 1423-1436, 1971.

24 Mathieu, R., and Bariac, T.: A numerical model for the simulation of stable isotope profiles in
25 drying soils, 101, 12685–12696, *J. Geophys. Res.-Atmos.*, doi: 10.1029/96jd00223, 1996

26 Merz, S., Pohlmeier, A., Vanderborght, J., van Dusschoten, D., and Vereecken, H.: Moisture
27 profiles of the upper soil layer during evaporation monitored by NMR, *Water Resour. Res.*,
28 50, 5184-5195, doi: 10.1002/2013wr014809, 2014.

29 Murray, F. W.: On the Computation of Saturation Vapor Pressure, *J. Appl. Meteorol.*, 6, 203-
30 204, doi: 10.1175/1520-0450, 1967.

1 Nash, J. E., and Sutcliffe, J. V.: River flow forecasting through conceptual models part I -A
2 discussion of principles, *Journal of Hydrology*, 10, 282-290, doi:10.1016/0022-
3 1694(70)90255-6, 1970

4 Oerter, E., Finstad, K., Schaefer, J., Goldsmith, G. R., Dawson, T., and Amundson, R.:
5 Oxygen isotope fractionation effects in soil water via interaction with cations (Mg, Ca, K, Na)
6 adsorbed to phyllosilicate clay minerals, *J. Hydrol.*, 515, 1-9, doi:
7 10.1016/j.jhydrol.2014.04.029, 2014.

8 Peng, T. R., Lu, W. C., Chen, K. Y., Zhan, W. J., and Liu, T. K.: Groundwater-recharge
9 connectivity between a hills-and-plains' area of western Taiwan using water isotopes and
10 electrical conductivity, *J. Hydrol.*, 517, 226-235, doi: 10.1016/j.jhydrol.2014.05.010, 2014.

11 Phillips, D. L., and Gregg, J. W.: Uncertainty in source partitioning using stable isotopes,
12 *Oecologia*, 127, 171-179, doi: 10.1007/s004420000578, 2001.

13 Rothfuss, Y., Biron, P., Braud, I., Canale, L., Durand, J. L., Gaudet, J. P., Richard, P.,
14 Vauclin, M., and Bariac, T.: Partitioning evapotranspiration fluxes into soil evaporation and
15 plant transpiration using water stable isotopes under controlled conditions, *Hydrol. Process.*,
16 24, 3177-3194, doi: 10.1002/Hyp.7743, 2010.

17 Rothfuss, Y., Braud, I., Le Moine, N., Biron, P., Durand, J. L., Vauclin, M., and Bariac, T.:
18 Factors controlling the isotopic partitioning between soil evaporation and plant transpiration:
19 Assessment using a multi-objective calibration of SiSPAT-Isotope under controlled
20 conditions, *J. Hydrol.*, 442, 75-88, doi: 10.1016/j.jhydrol.2012.03.041, 2012.

21 Rothfuss, Y., Vereecken, H., and Brüggemann, N.: Monitoring water stable isotopic
22 composition in soils using gas-permeable tubing and infrared laser absorption spectroscopy,
23 *Water Resour. Res.*, 49, 1-9, doi: 10.1002/wrcr.20311, 2013.

24 Schmidt, M., Maseyk, K., Lett, C., Biron, P., Richard, P., Bariac, T., and Seibt, U.:
25 Concentration effects on laser-based d18O and d2H measurements and implications for the
26 calibration of vapour measurements with liquid standards, *Rapid Commun. Mass Spectrom.*,
27 24, 3553-3561, doi: 10.1002/rcm.4813, 2010.

28 Shahraeeni, E., Lehmann, P., and Or, D.: Coupling of evaporative fluxes from drying porous
29 surfaces with air boundary layer: Characteristics of evaporation from discrete pores, *Water*
30 *Resour. Res.*, 48, doi: 10.1029/2012wr011857, 2012.

1 Singleton, M. J., Sonnenthal, E. L., Conrad, M. E., DePaolo, D. J., and Gee, G. W.:
2 Multiphase reactive transport modeling of seasonal infiltration events and stable isotope
3 fractionation in unsaturated zone pore water and vapor at the Hanford site, *Vadose Zone J.*, 3,
4 775-785, doi: 10.2113/3.3.775, 2004.

5 Sofer, Z., and Gat, J. R.: Activities and Concentrations of O-18 in Concentrated Aqueous Salt
6 Solutions - Analytical and Geophysical Implications, *Earth Planet. Sc. Lett.*, 15, 232-&, doi:
7 10.1016/0012-821x(72)90168-9, 1972.

8 Stingaciu, L. R., Pohlmeier, A., Blumler, P., Weihermuller, L., van Dusschoten, D., Stapf, S.,
9 and Vereecken, H.: Characterization of unsaturated porous media by high-field and low-field
10 NMR relaxometry, *Water Resour. Res.*, 45, doi: 10.1029/2008wr007459, 2009.

11 Sutanto, S. J., Wenninger, J., Coenders-Gerrits, A. M. J., and Uhlenbrook, S.: Partitioning of
12 evaporation into transpiration, soil evaporation and interception: a comparison between
13 isotope measurements and a HYDRUS-1D model, *Hydrol. Earth Syst. Sc.*, 16, 2605-2616,
14 doi: 10.5194/hess-16-2605-2012, 2012.

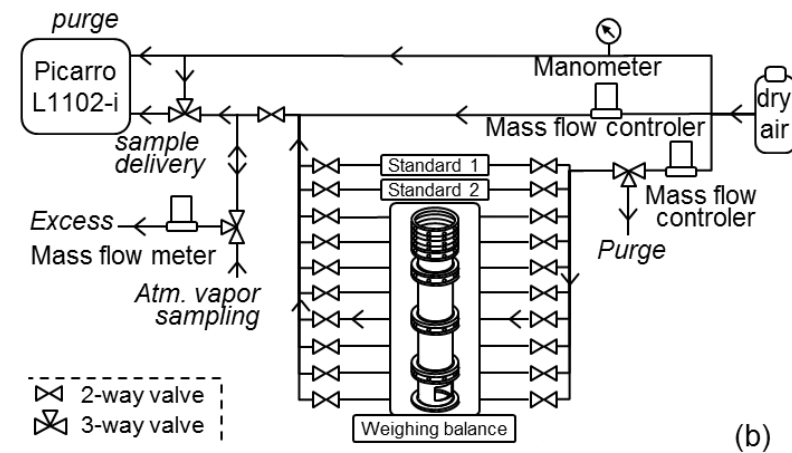
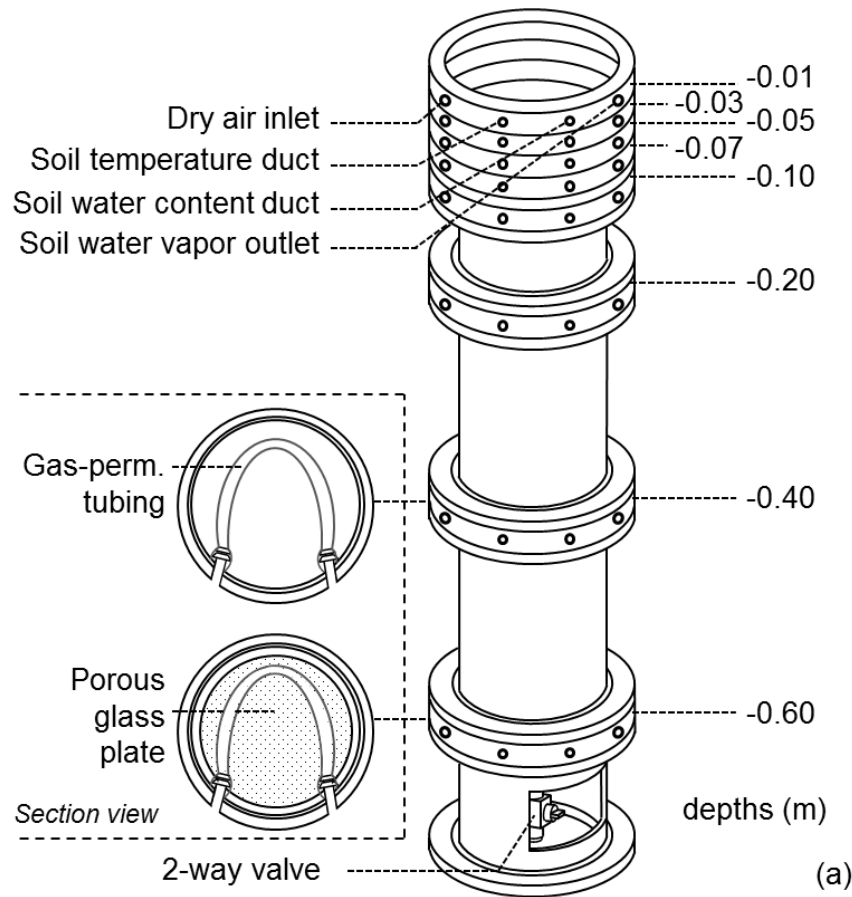
15 Volkmann, T. H. M., and Weiler, M.: Continual in situ monitoring of pore water stable
16 isotopes in the subsurface, *Hydrol. Earth Syst. Sc.*, 18, 1819-1833, doi: 10.5194/hess-18-
17 1819-2014, 2014.

18 Wang, P., Song, X. F., Han, D. M., Zhang, Y. H., and Liu, X.: A study of root water uptake of
19 crops indicated by hydrogen and oxygen stable isotopes: A case in Shanxi Province, China,
20 *Agric. Water Manage.*, 97, 475-482, doi: 10.1016/j.agwat.2009.11.008, 2010.

21 Yopez, E. A., Huxman, T. E., Ignace, D. D., English, N. B., Weltzin, J. F., Castellanos, A. E.,
22 and Williams, D. G.: Dynamics of transpiration and evaporation following a moisture pulse in
23 semiarid grassland: A chamber-based isotope method for partitioning flux components, *Agr.*
24 *Forest Meteorol.*, 132, 359-376, doi: 10.1016/j.agrformet.2005.09.006, 2005.

25 Zimmermann, U., Ehhalt, D., and Münnich, K. O.: Soil water movement and
26 evapotranspiration: changes in the isotopic composition of the water, *Symposium of Isotopes*
27 *in Hydrology*, Vienna, 1967, 567-584.

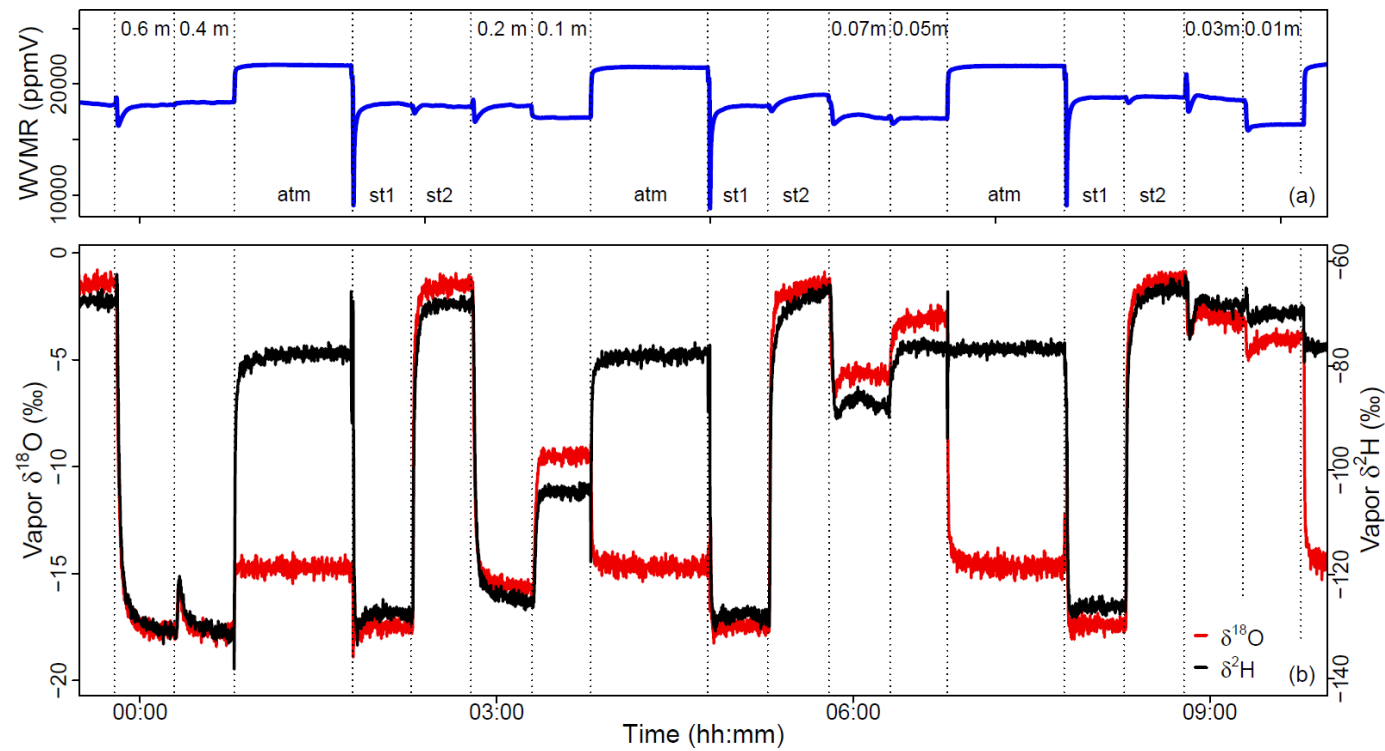
1 **Figures**



2

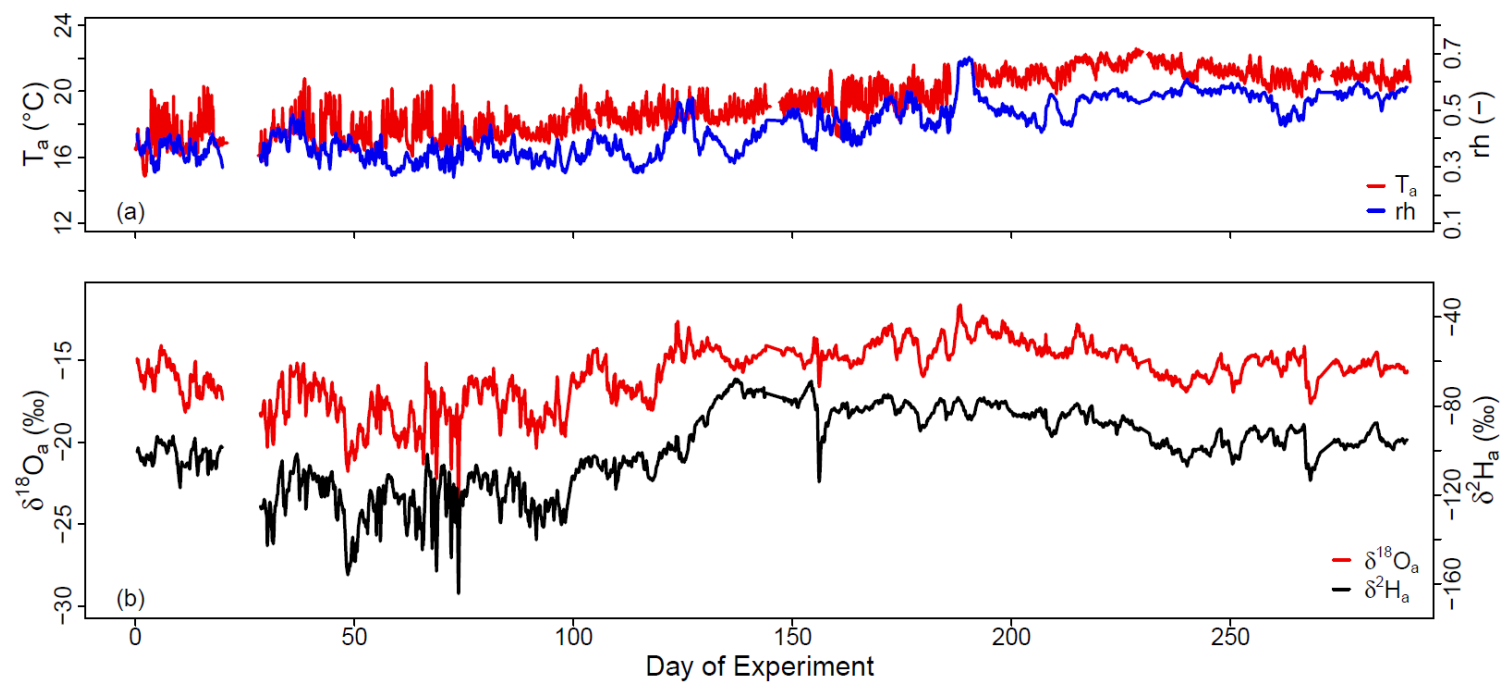
3 Figure 1. (a) Scheme of the acrylic glass column used in the experiment; (b) experimental setup for sampling water vapor at the different soil
 4 depths of the soil column, from the ambient air, and from the two soil water standards (standard 1 and 2)

5



1
2
3
4
5

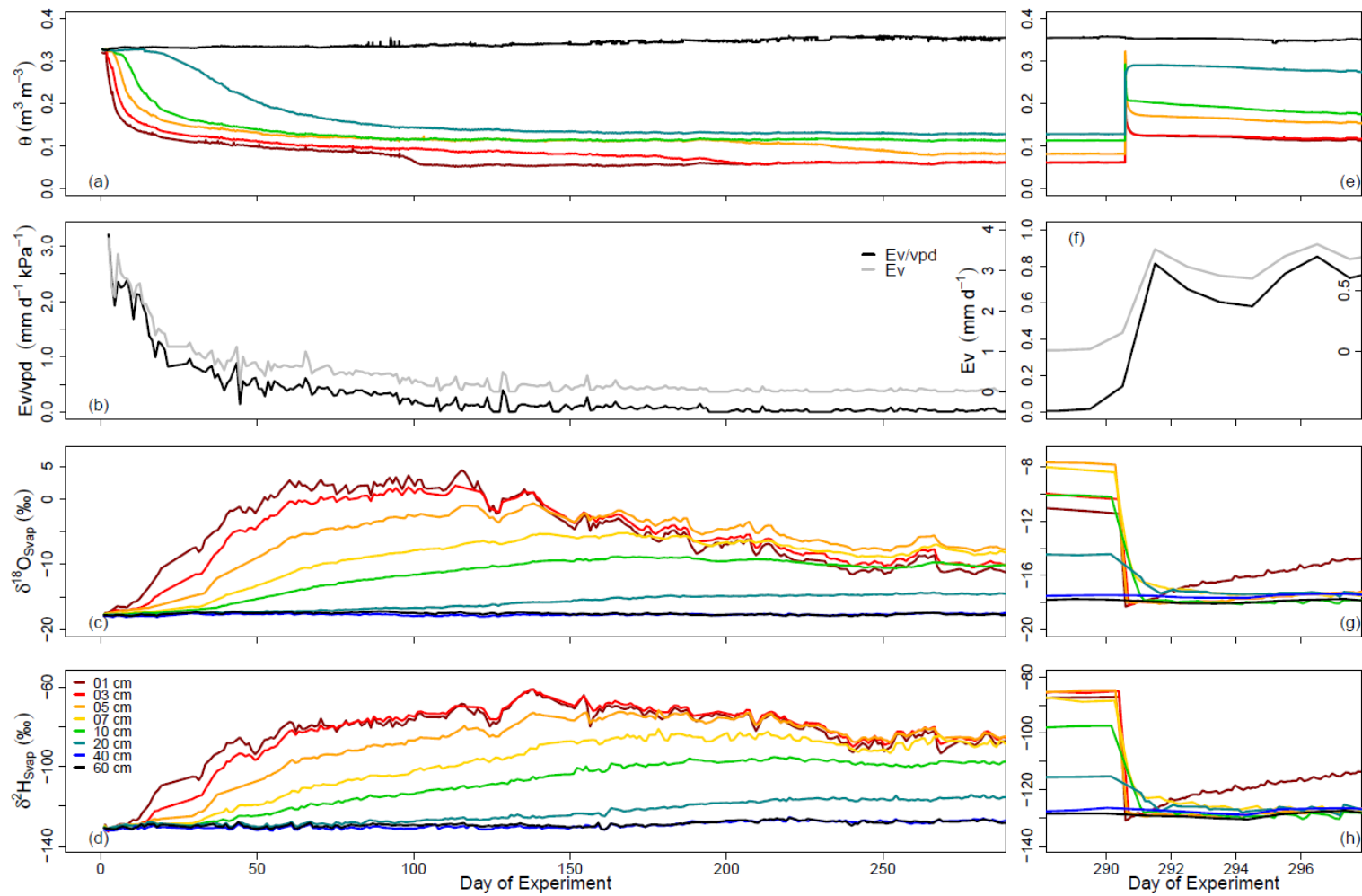
Figure 2. Water vapor mixing ratio (*WVMR*, in ppmv) and isotope composition ($\delta^{18}\text{O}$ and $\delta^2\text{H}$, in ‰ V-SMOW) of the water vapor sampled on Day of Experiment 150 from the ambient air (“atm”), both standards (“st1” and “st2”), and from the tubing sections at soil depths 1, 3, 5, 7, 10, 20, 40, and 60 cm



1

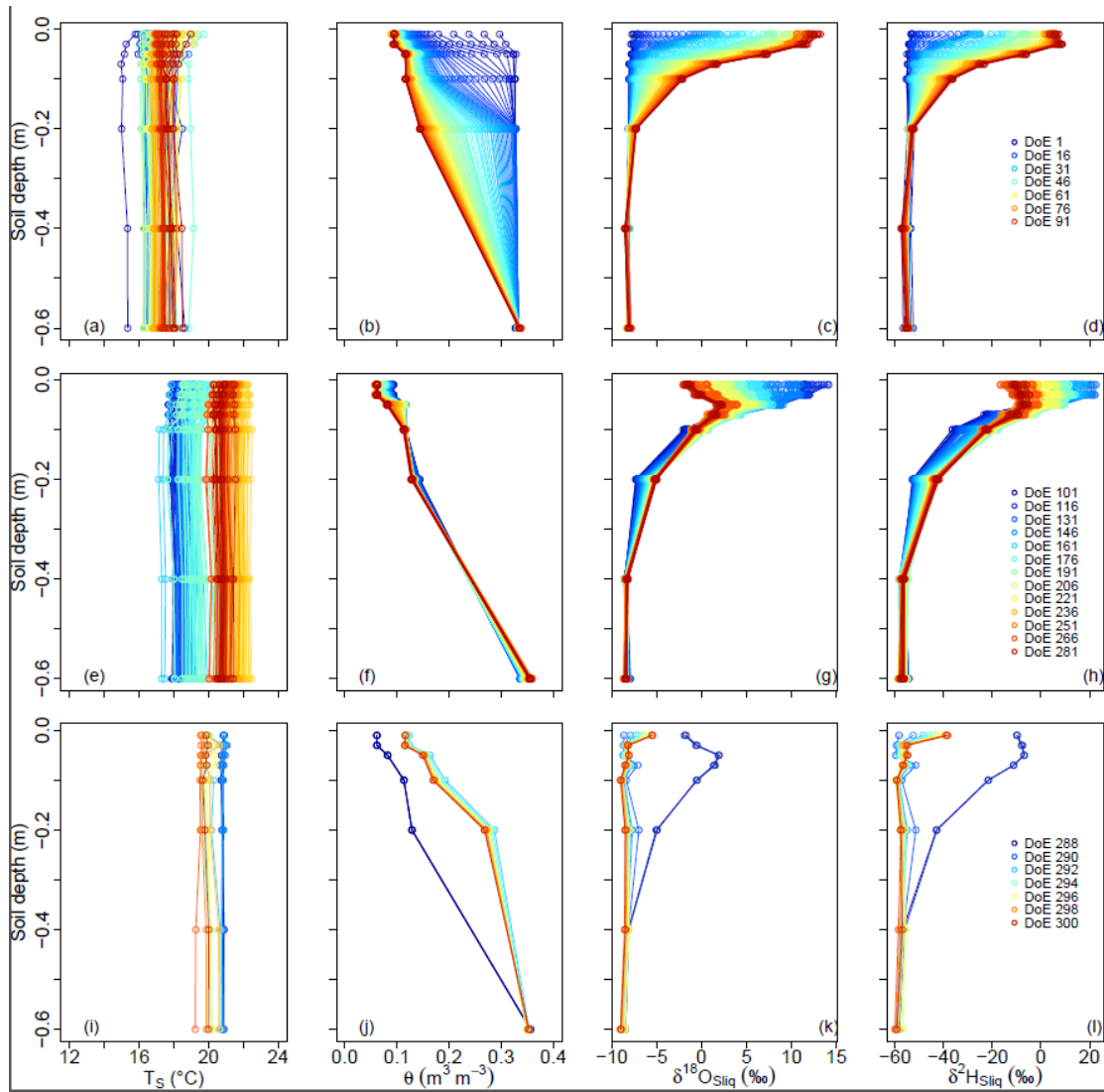
2 Figure 3. Time series of the laboratory ambient air temperature (T_a , in $^{\circ}\text{C}$), relative humidity (rh , in %) and water vapor isotope compositions
 3 ($\delta^{18}\text{O}_a$ and $\delta^2\text{H}_a$, in ‰ V-SMOW) over the course of the experiment

4



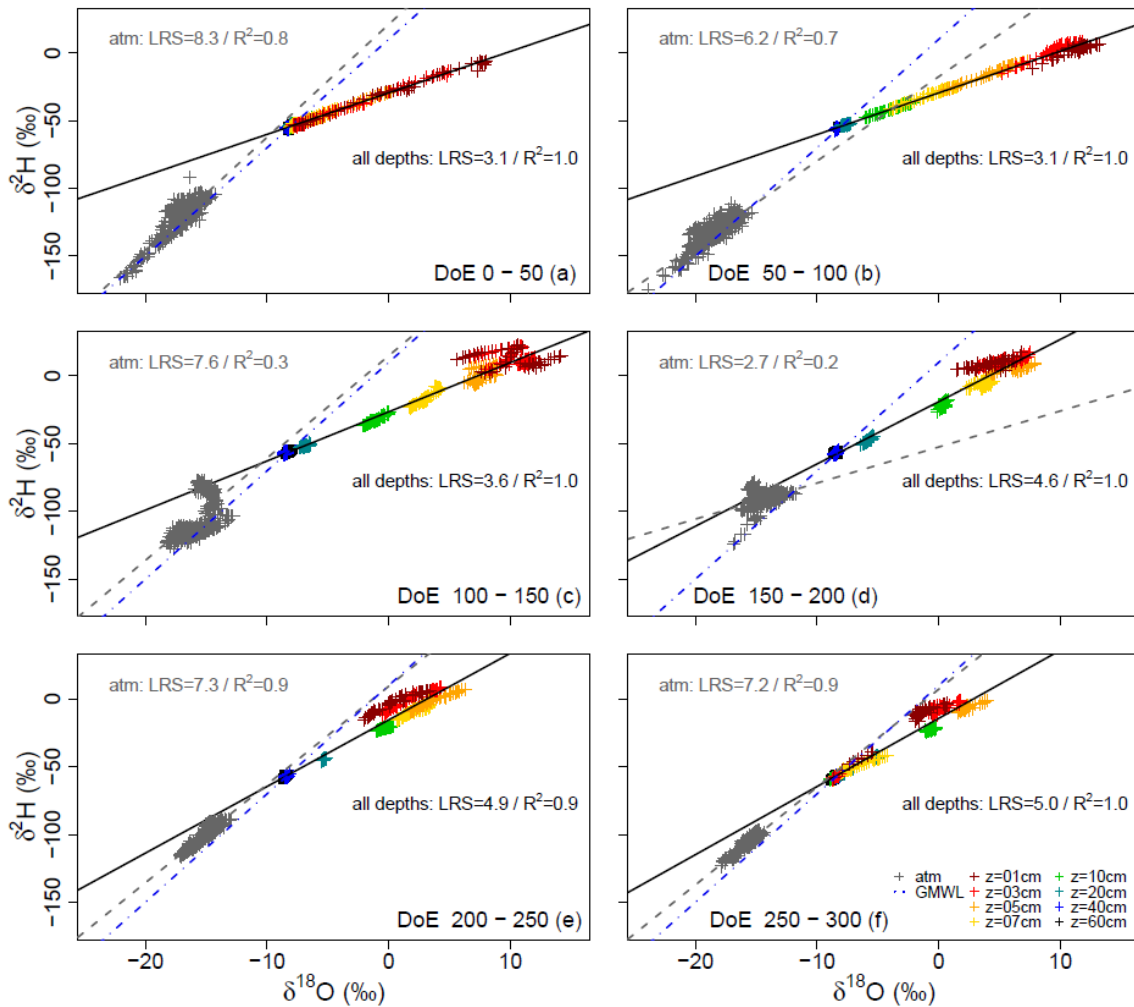
1

2 Figure 4. Time series of water content (θ , in $\text{m}^3 \text{m}^{-3}$), evaporation flux (Ev , in mm d^{-1}), and water vapor isotope compositions ($\delta^{18}\text{O}_{\text{Svap}}$ and
 3 $\delta^2\text{H}_{\text{Svap}}$, in ‰ V-SMOW) during the course of the experiment



1
 2 Figure 5. Soil temperature (T_S , in $^{\circ}\text{C}$), water content (θ , in $\text{m}^3 \text{m}^{-3}$), and liquid water isotope
 3 compositions ($\delta^{18}\text{O}_{\text{Sliq}}$ and $\delta^2\text{H}_{\text{Sliq}}$, in ‰ V-SMOW) profiles from Day of Experiment (DoE) 0
 4 - 100 (top panel), from DoE 101 - 287 (middle panel), and from DoE 288 - 299 (bottom
 5 panel)

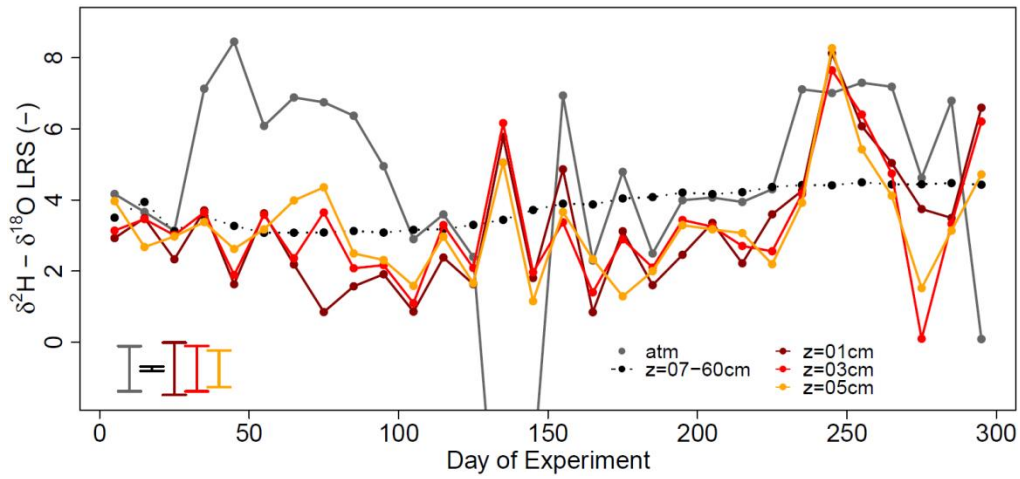
6



1

2 Figure 6. Linear regressions (gray dotted line) between laboratory atmosphere water vapor
 3 $\delta^{18}\text{O}$ and $\delta^2\text{H}$ (in ‰ V-SMOW) and between soil water $\delta^{18}\text{O}$ and $\delta^2\text{H}$ (solid black line). Each
 4 plot represents data from 50 consecutive days of experiment (DoE). Global Meteoric Water
 5 Line (GMWL, define by $\delta^2\text{H} = 8 * \delta^{18}\text{O} + 10$, in blue dotted line) is shown on each sub-plot for
 6 comparison. Coefficient of determination (R^2) as well as the slope of the linear regressions
 7 (LRS) are reported

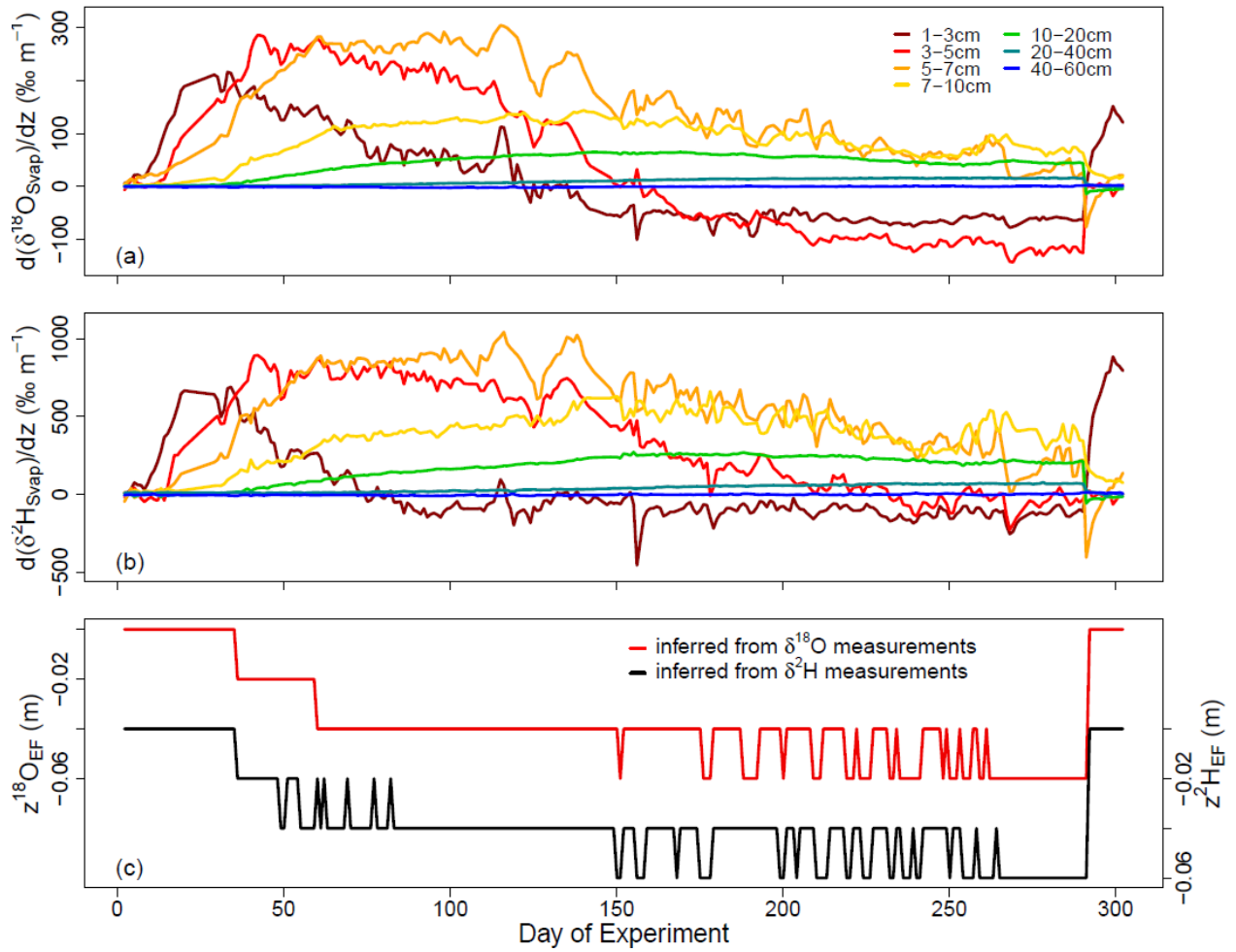
8



1

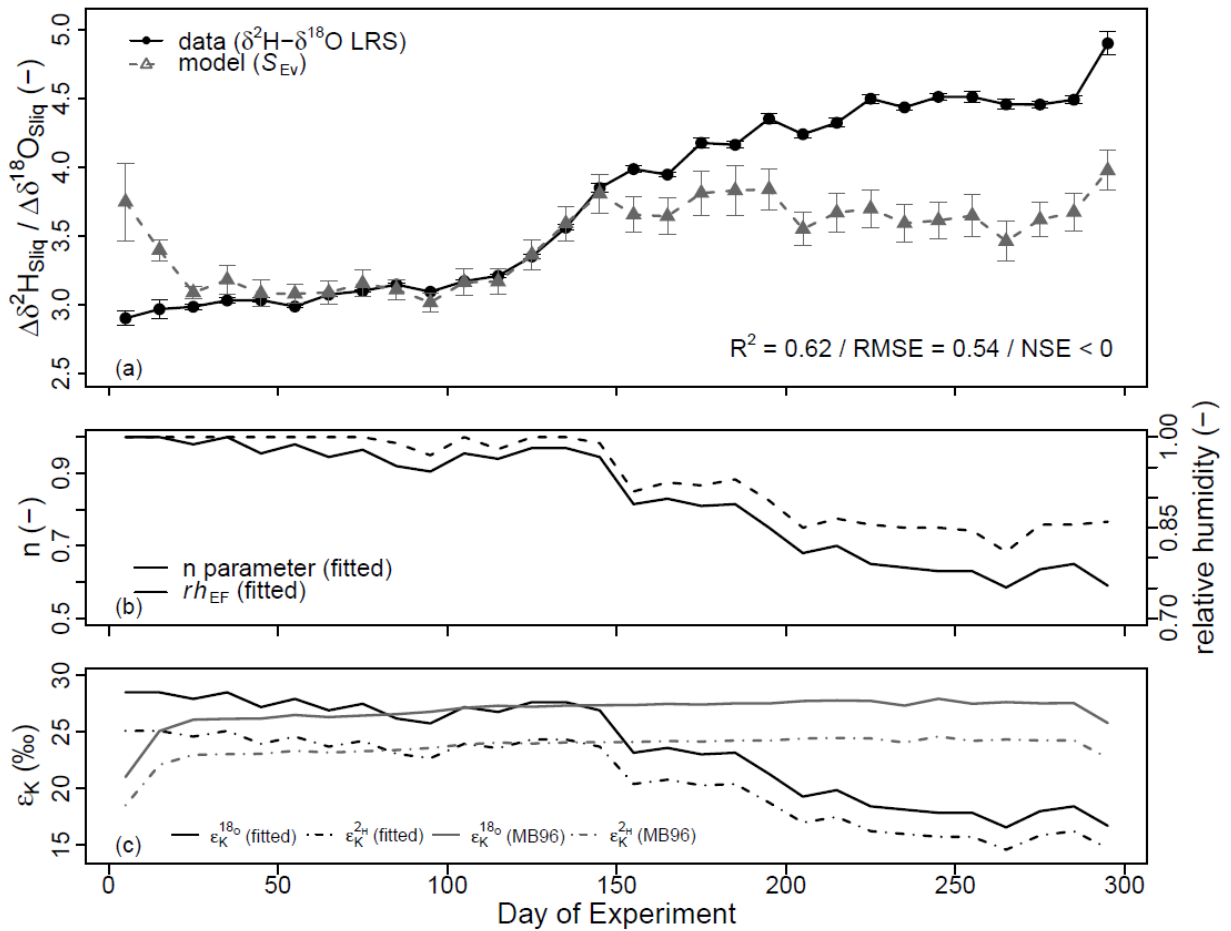
2 Figure 7. Time course of the slopes of the $\delta^{18}\text{O}$ - $\delta^2\text{H}$ linear regressions (LRS) for time
 3 intervals of ten consecutive days of atmosphere data (gray solid line), soil data from the upper
 4 three layers (01, 03, and 05 cm, colored solid lines), and combined soil data from the
 5 remaining bottom layers (from 07 to 60 cm, black dotted line). Mean standard errors are
 6 represented by the error bars in the bottom left corner

7



1
2
3
4
5
6

Figure 8. (a) and (b) $^1\text{H}^2\text{H}^{16}\text{O}$ and $^1\text{H}_2^{18}\text{O}$ composition gradients calculated between consecutive observation points in the soil. (c) Evolution of the evaporation front depths $z^{18}\text{O}_{\text{EF}}$ (red solid line) and $z^2\text{H}_{\text{EF}}$ (black solid line) inferred from the $^1\text{H}^2\text{H}^{16}\text{O}$ and $^1\text{H}_2^{18}\text{O}$ composition gradients



1
2 Figure 9. (a) Comparison between soil liquid water $\delta^{18}\text{O}$ - $\delta^2\text{H}$ linear regressions slopes (LRS,
3 solid black line) calculated for time intervals of ten consecutive days and simulated time
4 series of evaporation line slope (S_{Ev} , dotted gray line) obtained from Equations (3-6) (Gat et
5 al., 1971, Merlivat, 1978, Mathieu and Bariac, 1996). Black error bars give the standard errors
6 of the estimated $\delta^{18}\text{O}$ - $\delta^2\text{H}$ LRS. Gray error bars are the standard errors associated with
7 calculation of S_{Ev} following Phillips and Gregg (2001). Coefficient of determination (R^2),
8 Root Mean Square Error (RMSE) and Nash and Sutcliffe Efficiency (NSE) between model
9 and data are reported. (b) Time series of n parameter (Eq. (6)) and soil relative humidity at the
10 Evaporation Front (rh_{EF}) that provided the best model-to-data fit. (c) $\varepsilon_{\text{K}}^{2\text{H}}$ and $\varepsilon_{\text{K}}^{18\text{O}}$ time series
11 obtained from fitted n values (“fitted”) and calculated following Mathieu and Bariac (1996)
12 (“MB96”)